

# Diluted three-dimensional random field Ising model at zero temperature with metastable dynamics

Xavier Illa\* and Eduard Vives†

*Departament d'Estructura i Constituents de la Matèria, Martí i Franquès 1, Facultat de Física, Universitat de Barcelona, 08028 Barcelona, Catalonia, Spain*

(Received 12 May 2006; revised manuscript received 21 June 2006; published 11 September 2006)

The influence of vacancy concentration on the behavior of the three-dimensional random field Ising model with metastable dynamics is studied. We have focused our analysis on the number of spanning avalanches which allows us a clear determination of the critical line where the hysteresis loops change from continuous to discontinuous. By a detailed finite-size scaling analysis we determine the phase diagram and numerically estimate the critical exponents along the whole critical line. Finally, we discuss the origin of the curvature of the critical line at high vacancy concentration.

DOI: [10.1103/PhysRevB.74.104409](https://doi.org/10.1103/PhysRevB.74.104409)

PACS number(s): 75.50.Lk, 75.40.Mg, 05.50.+q, 75.10.Nr

## I. INTRODUCTION

Externally driven systems at sufficiently low temperature often display rate-independent hysteresis. This out-of-equilibrium phenomenon occurs because intrinsic disorder creates multiple energy barriers that the system cannot overcome due to very weak thermal fluctuations.

The study of zero-temperature models with metastable dynamics has been very successful for understanding rate-independent hysteresis. A prototypical case is the random field Ising model (RFIM) with single spin-flip relaxation dynamics.<sup>1,2</sup> Although the model is formulated in terms of magnetic variables (external field  $H$  and magnetization  $m$ ), it can be applied to the study of many phenomena associated with low-temperature first-order phase transitions in disordered systems, e.g., martensitic transformations,<sup>3</sup> fluid adsorption in porous solids,<sup>4</sup> ferroelectrics,<sup>5</sup> etc.

Disorder is an intriguing concept; in the RFIM it is introduced via independent, quenched random fields on each lattice site, Gaussian-distributed with zero mean, and standard deviation  $\sigma$ . In real materials, disorder is much more complicated and includes features on all length scales: vacancies, interstitials, composition fluctuations, dislocations, strain fields, grain boundaries, sample surfaces, edges and corners, etc. Thus, it is interesting to add to the RFIM other sources of disorder, in order to see how nonequilibrium behavior is modified.

The goal of this paper is to study the diluted RFIM at  $T=0$  with metastable dynamics and to analyze the consequence of introducing a concentration  $c$  of quenched vacancies. The interplay between the two kinds of disorder (random fields and vacancies) will be at the origin of the properties of the  $\sigma$ - $c$  phase diagram.

One of the striking results concerning the RFIM with metastable dynamics, as already pointed out in the seminal paper of Sethna *et al.*,<sup>1</sup> is the occurrence of a critical point when the amount of disorder  $\sigma$  is increased. The  $m$  vs  $H$  hysteresis loops change from being discontinuous (as in a ferromagnet) when  $\sigma < \sigma_c$  to continuous (as in a spin glass) when  $\sigma > \sigma_c$ . This result was demonstrated using mean-field analysis and numerical simulations in three-dimensional (3D) systems. This problem was also studied within the renormalization group (RG) formalism.<sup>6,7</sup> Moreover, many

properties of the critical point have also been studied analytically on Bethe lattices.<sup>8–12</sup> Experimental evidence for the occurrence of such a critical point has been found in different magnetic systems.<sup>13,14</sup>

Another interesting result of the RFIM with metastable dynamics is that it reproduces the experimental observation that  $m(H)$  trajectories of such athermal systems are discontinuous on small scales. The evolution proceeds by avalanches from one metastable state to another. In the RFIM the avalanche-size distribution becomes a power law at the critical point. Experimentally, scale-free distributions of avalanche properties have been found in many systems.<sup>15–22</sup> A first attempt to study the influence of dilution in such avalanche-size distributions was done some years ago.<sup>23</sup> The results of this work, however, should be considered as only qualitative, given the fact that the studied system was two dimensional (2D),<sup>28</sup> the analysis only focused on the avalanche distributions and the results concerning the phase diagram were very approximate.

The order parameter that vanishes at the critical point is the size of the macroscopic discontinuity  $\Delta m$ . Analysis of this quantity from simulations is very intricate. In finite-size systems it is very difficult to make the distinction between a macroscopic jump and a microscopic avalanche. The measured-order parameter only displays reasonable finite-size scaling (FSS) properties when the simulated systems are very large.<sup>24</sup> Recent studies<sup>25,26</sup> have shown how the critical point can be characterized in systems of moderate size. The key point is to detect the so-called “spanning” avalanches, which are the magnetization jumps that involve a set of spins that spans the whole finite system (e.g., cubic lattice) from one face to the one opposite. By this method avalanches in finite systems can be classified as nonspanning, one-dimension (1D) spanning, 2D spanning, or 3D spanning. The average numbers  $N_1$ ,  $N_2$  of 1D- and 2D-spanning avalanches display a peak at a value of  $\sigma$  that shifts with system size  $L$  and tends to  $\sigma_c$  when  $L \rightarrow \infty$ . The numerical data can then be scaled according to the FSS hypothesis<sup>25</sup>

$$N_\alpha = L^\theta \tilde{N}_\alpha(uL^{1/\nu}), \quad (1)$$

where  $\alpha=1,2$ . The exponent  $\nu=1.2 \pm 0.1$  characterizes the divergence of the correlation length  $[\xi \sim (\sigma - \sigma_c)^{-\nu}]$ , while

$\theta=0.10\pm 0.02$  characterizes the divergence of the number of critical avalanches. The scaling variable  $u(\sigma)$  is analytic and measures the distance to the critical point. It can be fitted by the second-order expression

$$u(\sigma) = \frac{\sigma - \sigma_c}{\sigma_c} + A \left( \frac{\sigma - \sigma_c}{\sigma_c} \right)^2, \quad (2)$$

with  $\sigma_c=2.21$  and  $A=-0.2$ . The behavior of the 3D-spanning avalanches is more complex because there are two different kinds; (i) critical 3D-spanning avalanches that behave as the 1D and 2D avalanches and (ii) subcritical 3D-spanning avalanches which correspond to the  $\Delta m$  discontinuity in the thermodynamic limit. The analysis is more difficult and requires a double finite-size scaling technique. This will not be used in the present paper. Instead we will only focus on the behavior of the average numbers  $N_1$  and  $N_2$  in the presence of vacancies and propose a FSS hypothesis by using a scaling variable  $u(\sigma, c)$  that allows the full  $\sigma$ - $c$  diagram to be studied.

In Sec. II we define the model and the dynamics. In Sec. III we present results of the numerical simulations. In Sec. IV we formulate the FSS hypothesis and determine the critical line. In Sec. V we propose approximations to the scaling variable  $u(\sigma, c)$ . In Sec. VI, we discuss the interplay between vacancies and avalanches and, finally, in Sec. VII we summarize our main findings and conclude.

## II. MODEL AND SIMULATIONS

The diluted 3D RFIM on a cubic lattice with  $N$  sites ( $N=L\times L\times L$ ) is defined by the following Hamiltonian (magnetic enthalpy):

$$\mathcal{H} = - \sum_{\langle ij \rangle}^{n.n.} c_i c_j S_i S_j - \sum_{i=1}^N h_i c_i S_i - H \sum_{i=1}^N S_i c_i, \quad (3)$$

where  $S_i = \pm 1$  are Ising spin variables,  $c_i = 0, 1$  indicates the presence of a vacancy ( $c_i = 0$ ) or not ( $c_i = 1$ ) at each site,  $h_i$  are Gaussian-distributed quenched random fields with zero

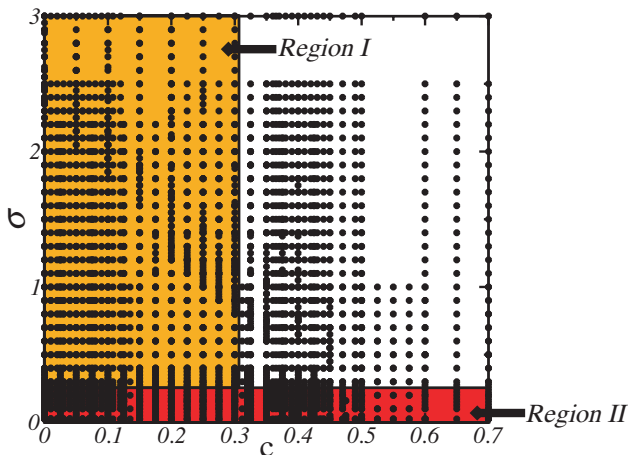


FIG. 1. (Color online) Coordinates of the points studied by numerical simulations on the  $\sigma$ - $c$  diagram. The finite-size scaling analysis presented in Sec. IV is performed in regions I and II.

mean and standard deviation  $\sigma$ , and  $H$  is the driving field. The first sum extends over all distinct nearest-neighbor ( $n.n.$ ) pairs. Vacancies are quenched and randomly distributed over the lattice. Their concentration is measured by  $c = 1 - \sum_i c_i / N$ .

The metastable dynamics is implemented as follows: the system is externally driven by the field  $H$  which is adiabatically swept from  $-\infty$  where the system is fully negatively magnetized ( $S_i = -1$ ) to  $+\infty$  ( $S_i = +1$ ). The spins flip according to a local relaxation dynamical rule

$$S_i = \text{sign} \left( \sum_j S_j c_j + h_i + H \right), \quad (4)$$

where the sum extends over all the  $n.n.$  of  $S_i$ . When a spin flips, it may trigger an avalanche. The unstable spins are flipped synchronously until a new stable situation is reached.

The hysteresis loop is obtained by computing the magnetization

$$m = \sum_{i=1}^N S_i c_i / N, \quad (5)$$

as a function of the applied field  $H$ . Magnetization avalanches are recorded along the whole increasing field branch and their spanning properties are analyzed by using “mask” vectors (as explained in Ref. 25) that allow them to be classified as nonspanning, 1D spanning, 2D spanning, and 3D spanning. In this work we shall mainly study the number of spanning avalanches of each kind which are recorded in the full upwards branch. These numbers,  $N_1$ ,  $N_2$ , and  $N_3$ , which depend on  $L$ ,  $\sigma$ , and  $c$ , correspond to averages over more than  $10^4$  realizations with different random fields and random vacancy positions. The disorder averages are denoted by the symbol  $\langle \cdot \rangle$ . We study systems of sizes ranging from  $L=8$  to  $L=64$  at a number of points on the  $\sigma$ - $c$  diagram, as indicated schematically in Fig. 1.

## III. NUMERICAL RESULTS

The general evolution of the average hysteresis loops as a function of  $\sigma$  and  $c$  is shown in Fig. 2. One can observe the transition from discontinuous loops to smooth loops when  $\sigma$  or  $c$  are increased. It can also be seen that the saturation magnetization decreases with increasing  $c$ .

Figure 3 shows the behavior of the coercive field  $\langle H_{coe} \rangle$  as a function of the concentration of vacancies for different values of  $\sigma$ . As can be seen,  $\langle H_{coe} \rangle$  decreases with increasing  $c$  and increasing  $\sigma$ . The behavior with increasing  $c$  exhibits an inflection point at the transition, as can be seen in the inset of Fig. 3, which shows the numerical derivative of the  $\langle H_{coe} \rangle$  with respect to  $c$ . Such an inflection point does not exist in the nondiluted model when the coercive field is plotted as a function of  $\sigma$ . This feature, which can be of interest for the determination of the critical point in experiments, is probably related to the fact that  $\langle H_{coe} \rangle$ , expressed as a function of  $c$ , should vanish at  $c \leq 1$ , whereas if it is expressed as a function of  $\sigma$  it only vanishes asymptotically when  $\sigma \rightarrow \infty$ .

Figure 4 shows the distribution  $D(s; \sigma, c, L)$  of avalanche sizes (the size  $s$  of an avalanche is the number of spins

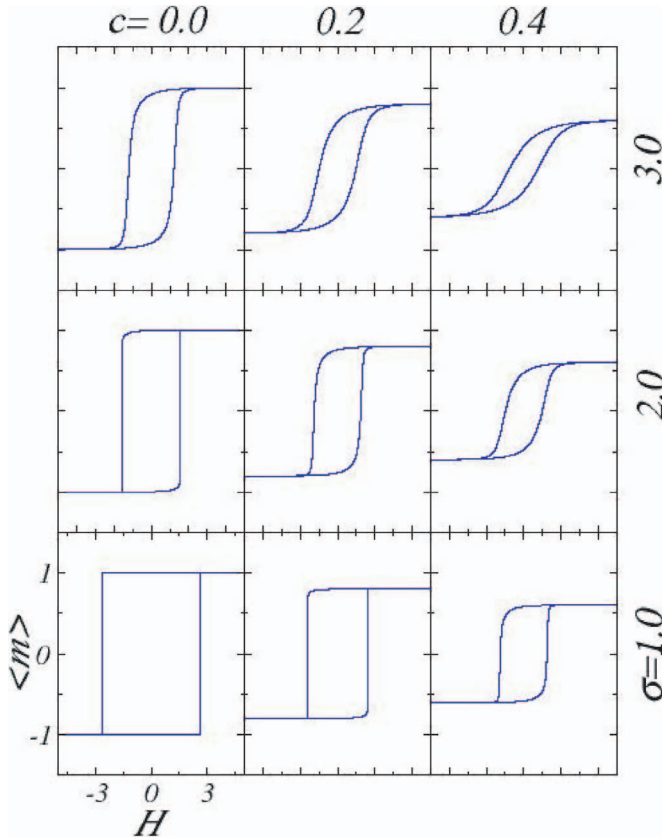


FIG. 2. (Color online) Average hysteresis loops corresponding to a system of size  $L=32$  for different values of  $\sigma$  and  $c$  as indicated.

flipped) for the same cases as in Fig. 2 on the log-log scale. The histograms include all avalanches irrespective of their spanning properties. The qualitative picture is that power-law distributions are obtained along a critical line with an expo-

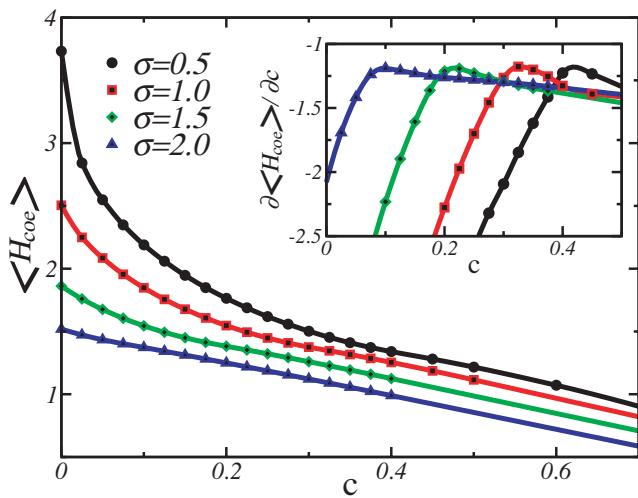


FIG. 3. (Color online) The coercive field as a function of the vacancy concentration  $c$  for different values of the amount of disorder  $\sigma$ . The inset shows the behavior of the numerical derivative  $\partial H_{coe} / \partial c$  which exhibits a maximum at the transition line. Data correspond to averages in a system of size  $L=64$ .

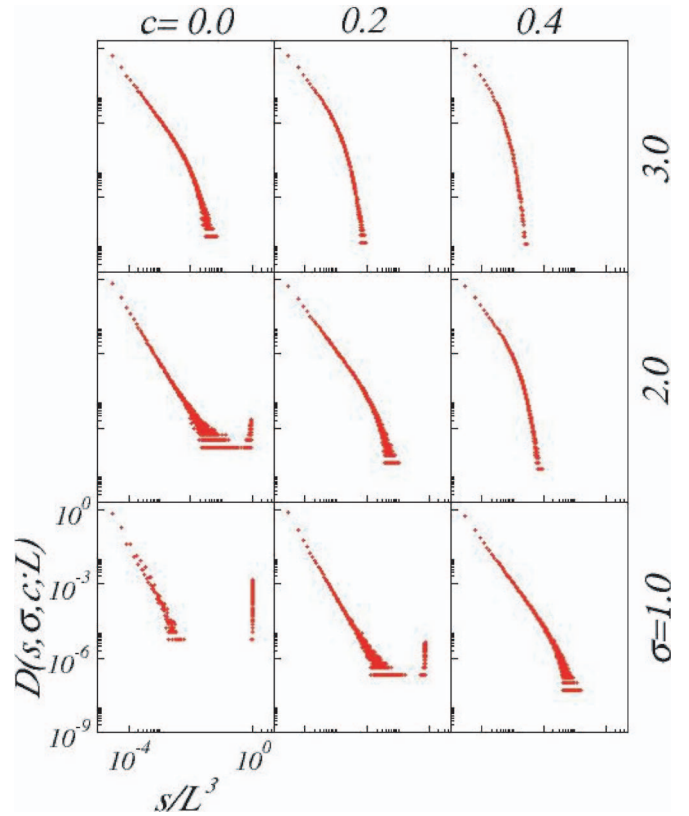


FIG. 4. (Color online) Avalanche size distributions corresponding to a system with  $L=32$  at different values of  $c$  and  $\sigma$  as indicated. Data are represented on the log-log scale.

nent that seems to be the same for all values of  $c$ . Apparently, no differences can be observed when comparing the transition induced by changing  $\sigma$  from the transition induced by changing  $c$ . Below the critical line the distributions show a peak for large values of  $s$  which correspond to the 1D-, 2D-, and 3D-spanning avalanches. Above the critical line, the distributions have an exponentially damped character.

Figure 5 shows the average number of 1D-, 2D-, and 3D-spanning avalanches as a function of  $\sigma$  for increasing values of the vacancy concentration  $c$  ranging from 0 to 0.5. Data correspond to a system with size  $L=16$ . The same information is displayed in Fig. 6 for a system with size  $L=48$ .

The behavior for small and intermediate vacancy concentration is qualitatively similar to that found for the nondiluted model.<sup>25,27,28</sup> The average numbers  $N_1$  and  $N_2$  display peaks, whereas  $N_3$  shows a peak on the edge of a step function. Note that for  $L=16$  the peak height in  $N_1(\sigma, c, L)$  and  $N_2(\sigma, c, L)$  seems to decrease with increasing  $c$ . This behavior, however, is much less apparent for larger systems ( $L=48$ ). Therefore, it is possibly due to a finite-size effect.

At higher concentrations ( $c > 0.4$ )  $N_1$  and  $N_2$  begin to develop a flat plateau at low  $\sigma$ . The reason for this plateau can be well understood by looking at the 3D plot in Fig. 7, which represents the average number  $N_1(\sigma, c, L)$  for  $L=32$ . The plateau in the constant  $c$  cuts of Figs. 5 and 6 is due to the fact that the crest of the  $N_1$  and  $N_2$  functions does not decrease linearly with increasing  $c$ , but shows a bend and reaches the  $c$  axis almost perpendicularly.

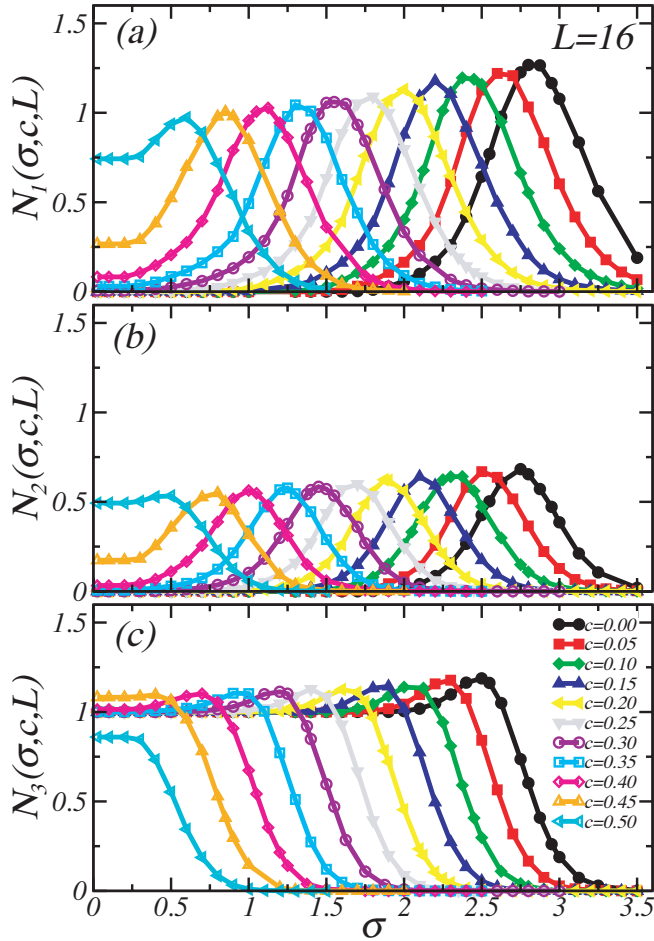


FIG. 5. (Color online) Average number of (a) 1D-spanning avalanches, (b) 2D-spanning avalanches, and (c) 3D-spanning avalanches, as a function of  $\sigma$  for different values of the vacancy concentration  $c$ , as indicated by the legend. Lines are guides to the eye. Data correspond to numerical simulations of a system with size  $L=16$ .

#### IV. FINITE-SIZE SCALING HYPOTHESIS

The hypothesis that we want to check numerically is that in the presence of vacancies, the critical point found at  $c=0$  transforms into a critical line for a wide range of concentrations. Thus, the critical exponents found previously should be equally valid for the description of the behavior of the average numbers  $N_1$  and  $N_2$  with  $c>0$ . According to this hypothesis we shall propose the following corresponding FSS behavior:

$$N_\alpha(\sigma, c, L) = L^\theta \tilde{N}_\alpha(uL^{1/\nu}), \quad (6)$$

where  $\alpha=1, 2$  and  $u(\sigma, c)$  is a scaling variable that measures the distance to the critical line. The exponents  $\theta$  and  $\nu$ , as well as the functions  $\tilde{N}_\alpha$ , were already found in previous works.<sup>25</sup> Therefore, the hypothesis is quite strong and indicates that all the  $N_1$  and  $N_2$  data, corresponding to different sizes  $L$ , different vacancy concentrations  $c$ , and different amounts of disorder  $\sigma$ , must collapse onto a function that is already known. The only freedom that we have is in the determination of the scaling variable  $u$  that should be an-

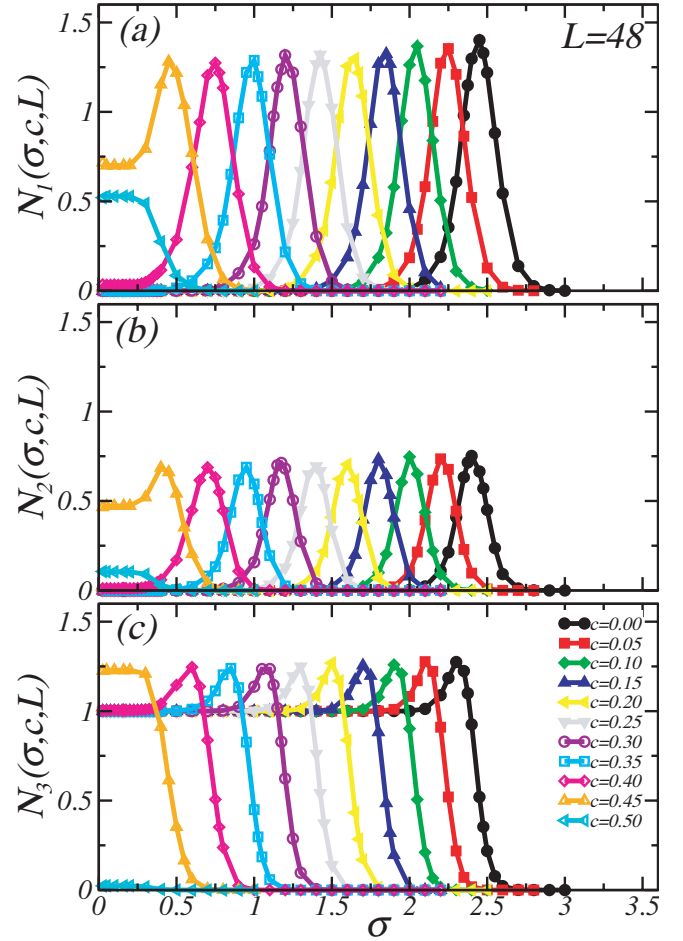


FIG. 6. (Color online) Average number of (a) 1D-spanning avalanches, (b) 2D-spanning avalanches, and (c) 3D-spanning avalanches, as a function of  $\sigma$  for different values of the vacancy concentration  $c$ , as indicated by the legend. Lines are guides to the eye. Data correspond to numerical simulations of a system with size  $L=48$ .

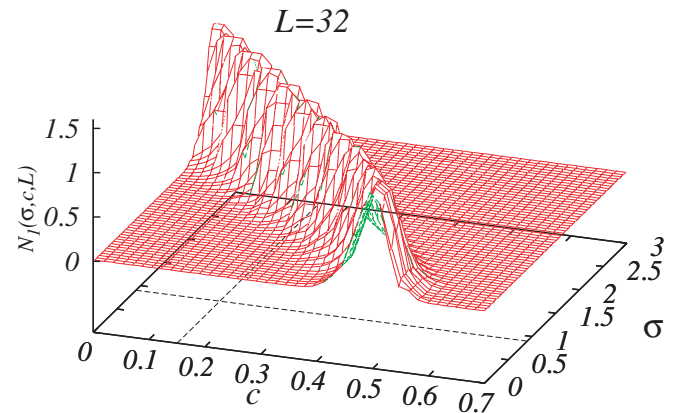


FIG. 7. (Color online) Surface plot representing  $N_1(\sigma, c, L)$  for  $L=32$ . The dashed lines on the basal plane represent the position of the cuts in Fig. 8 at  $c=0.15$  and  $\sigma=0.9$ .

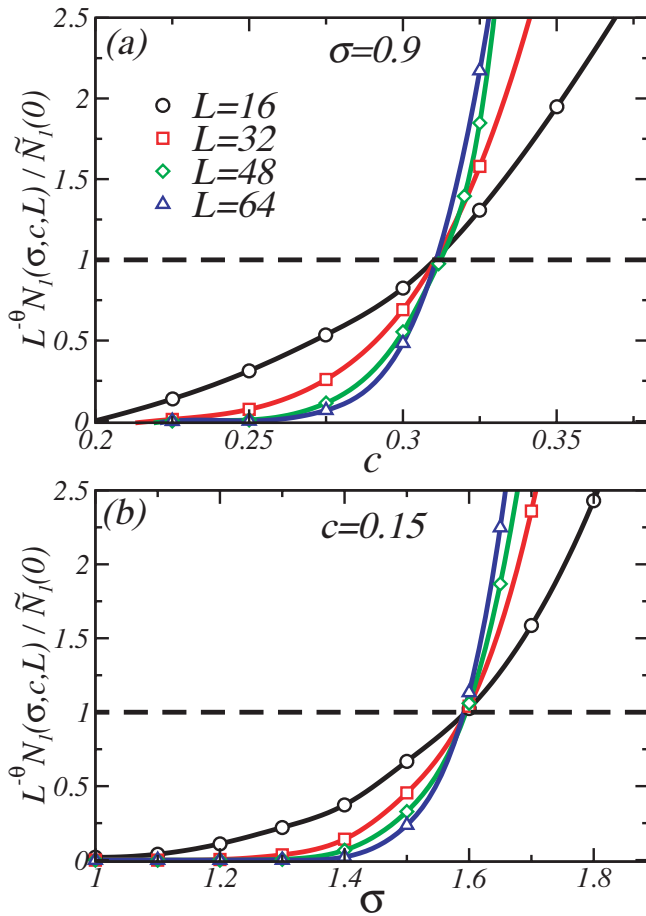


FIG. 8. (Color online) Examples of crossing points on the critical line along cuts (a) parallel to the  $c$  axis and (b) parallel to the  $\sigma$  axis. The different symbols correspond to different system sizes as indicated by the legend. Continuous lines are guides to the eye. The horizontal dashed line indicates the height 1 where the curves are supposed to cross according to Eq. (7).

lytic. Before constructing it in the next section, we can make a first test of Eq. (6) by checking scaling on the critical line. Note that by setting  $u=0$ , Eq. (6) becomes

$$N_{\alpha}(\sigma, c, L) = L^{\theta} \tilde{N}_{\alpha}(0), \quad (7)$$

where  $\sigma$  and  $c$  should be on the critical line. Since we know (from Ref. 25) that  $\theta=0.10$ ,  $\tilde{N}_1(0)=0.12$ , and  $\tilde{N}_2(0)=0.07$ , we can deduce that the different curves  $N_{\alpha}(\sigma, c, L)/L^{\theta} \tilde{N}_{\alpha}(0)$  should cross at height 1 on the critical line, independently of  $L$ . Two examples are shown in Fig. 8 that correspond to two cuts (one at constant  $\sigma$  and the other at constant  $c$ ) on the  $\sigma$ - $c$  diagram. As can be seen, the critical line can be determined to high accuracy. By analyzing a large number of such  $\sigma$  and  $c$  cuts, we have managed to construct the critical line. The result is shown in Fig. 9. Note that the process can be repeated independently with  $N_1$  and  $N_2$ . The two independent lines overlap almost perfectly. The obtained critical line is linear up to  $c \approx 0.3$ . A least-squares fit gives  $\sigma_c(c) = \sigma_c(0) + \lambda c$  with  $\sigma_c(0) = 2.21 \pm 0.01$  and  $\lambda = -4.09 \pm 0.03$ . The value

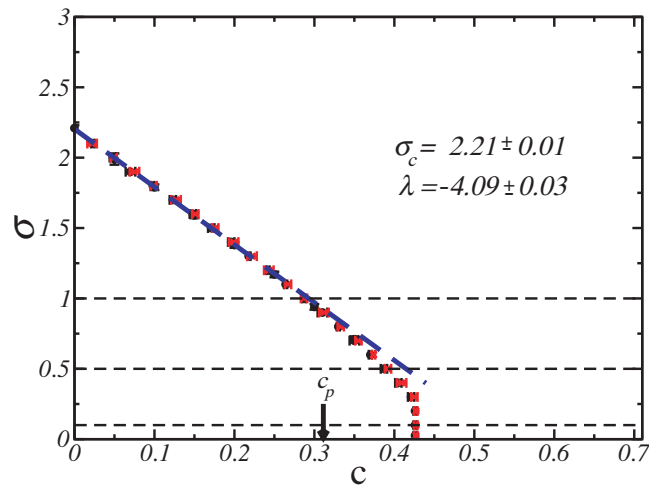


FIG. 9. (Color online) Critical line in the  $\sigma$ - $c$  diagram determined from the crossing points in  $N_1$  ( $\bullet$ ) and  $N_2$  ( $\times$ ). The dashed line is the fit discussed in the text, and the thin discontinuous lines indicate the cuts along which the correlation in Fig. 14 is computed.

$\sigma_c(0) = 2.21$  is in total agreement with the previous estimate for the nondiluted model.<sup>25</sup>

It is remarkable that the finite-size-scaling hypothesis allows the collapse of the data up to large values of  $c$ , far from the point  $c=0$ , where the scaling function and the exponents were determined. It is also remarkable that scaling works even after the bend observed for  $c > 0.3$ . [Note that the crossing point shown in Fig. 8(a) corresponds to a value of  $\sigma$  where the critical line is not linear.]

For small values of  $\sigma$  the critical line displays vertical behavior. The critical value of the vacancy concentration  $c_c$  above which the hysteresis loops do not display a discontinuity can be fitted to  $c_c = 0.426 \pm 0.003$ .

## V. SCALING VARIABLE

In general the scaling variable is a function that can be expanded as

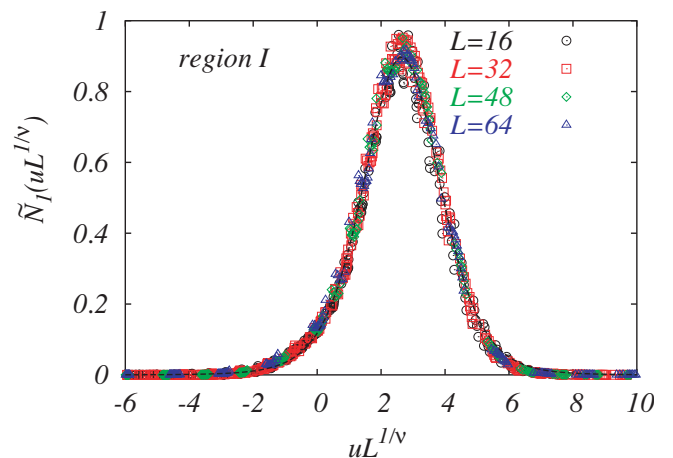


FIG. 10. (Color online) Finite-size-scaling collapse of the average number of 1D-spanning avalanches in region I. The continuous line shows the Lorentzian function in Eq. (12).

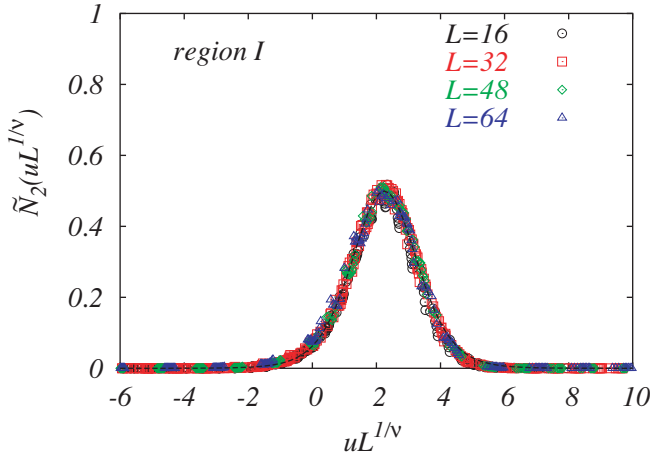


FIG. 11. (Color online) Finite-size-scaling collapse of the average number of 2D-spanning avalanches in region I. The continuous line shows the Lorentzian function in Eq. (13).

$$u(\sigma, c) = a_0 + a_1\sigma + a_2c + a_3\sigma c + a_4\sigma^2 + a_5c^2 + \dots \quad (8)$$

Since  $c$  and  $\sigma$  are not necessarily very small along the critical line, it is difficult to know *a priori* how many terms in the expansion will be needed in order to obtain a good scaling collapse. The direct determination of a large number of coefficients from the numerical data is difficult. Therefore, we shall adopt a different strategy by taking into account previously known data as much as possible.

As a first step we will concentrate on the region  $c \leq 0.3$  where the coexistence line shows linear behavior and we will try to use an expansion up to quadratic terms only. By forcing the condition  $u=0$  to be satisfied on the fitted coexistence line, we deduce that  $u$  satisfies

$$u(\sigma, c) = (\sigma - \sigma_c - \lambda c)(b_0 + b_1\sigma + b_2c). \quad (9)$$

We should also consider the fact that the scaling variable is known to be well described by a second-order expansion (up to  $\sigma^2$ ) for  $c=0$  as indicated in Eq. (2). After some algebra

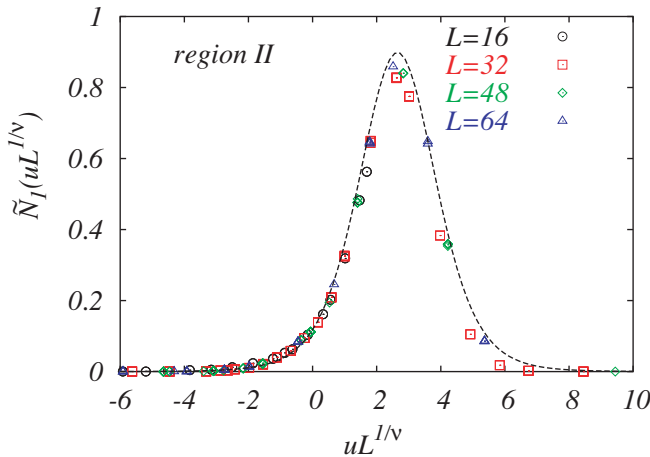


FIG. 12. (Color online) Finite-size-scaling collapse of the average number of 1D-spanning avalanches in region II. The continuous line shows the Lorentzian function in Eq. (12).

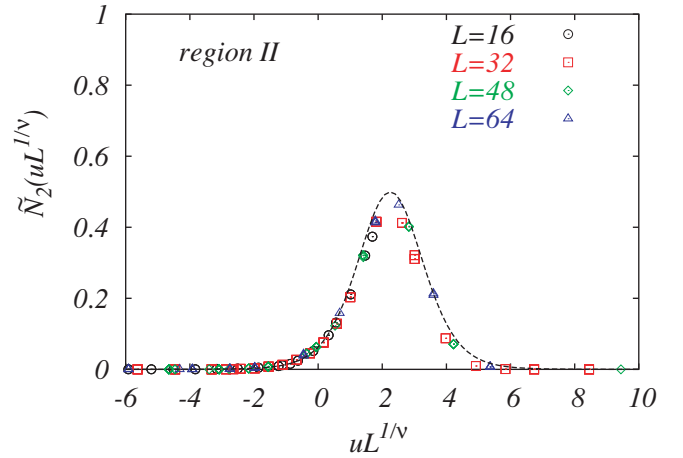


FIG. 13. (Color online) Finite-size scaling collapse of the average number of 2D-spanning avalanches in region II. The continuous line shows the Lorentzian function in Eq. (13).

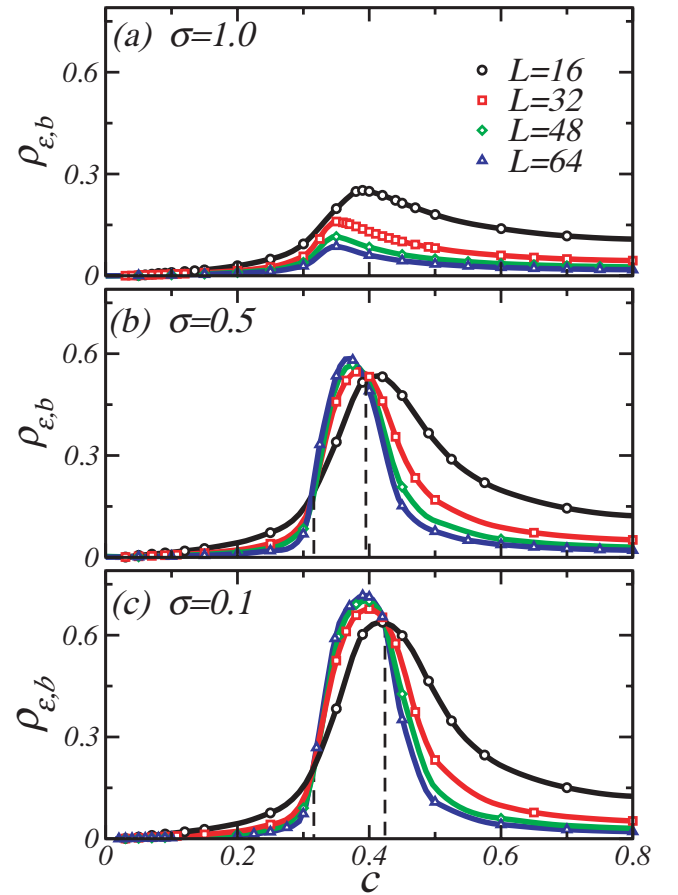


FIG. 14. (Color online) Correlation between the border of the largest cluster of vacancies and the largest avalanche as a function of  $c$ . Data corresponding to different system sizes are represented by different symbols as indicated by the legend. The curves correspond to cuts in the phase diagram at (a)  $\sigma=1$ , (b)  $\sigma=0.5$ , and (c)  $\sigma=0.1$ .

one can determine the two parameters  $b_0$  and  $b_1$ ,

$$b_0 = (1 - A)/\sigma_c = 0.543 \pm 0.002, \quad (10)$$

$$b_1 = A/\sigma_c^2 = -0.041 \pm 0.001. \quad (11)$$

Therefore, we are left with a single free parameter  $b_2$  that should allow all of the data in the scaling region to collapse onto a single curve for different values of  $\sigma$ ,  $c$ , and  $L$ . All the available data in region I of Fig. 1 have been considered. Note also that the same  $b_2$  parameter must be used to scale both  $N_1$  and  $N_2$  data. The best two collapses are shown in Figs. 10 and 11 for  $b_2 = -0.13$ . Note that the data for  $c=0$  are also included on this plot. Therefore, we have obtained two scaling functions  $\tilde{N}_1$  and  $\tilde{N}_2$  that are compatible with those of Ref. 25. In this paper the scaling functions were approximated by Gaussians, although it was also shown that there were systematic deviations. In this work we have tried to fit the data using more complex functions (with three free parameters). We have found a very good  $\chi^2$  by using the following modified Lorentzians, which are represented by a continuous line on the data in Figs. 10 and 11,

$$\tilde{N}_1(x) = \frac{1}{(1.73 - 0.53x + 0.10x^2)^{3.9}}, \quad (12)$$

$$\tilde{N}_2(x) = \frac{1}{(1.83 - 0.59x + 0.13x^2)^{4.6}}. \quad (13)$$

For a second step we will try to build up  $u(\sigma, c)$  for the data very close to the  $\sigma=0$  axis. In this region II (see Fig. 9) the transition line is again quite linear and, in fact, is almost vertical. This means that to measure the distance to the critical line it should be sufficient to use the variable  $(c - c_c)$ . We have considered the following second-order expansion:

$$\frac{u(c)}{k'} = \frac{c - c_c}{c_c} + B \left( \frac{c - c_c}{c_c} \right)^2. \quad (14)$$

Note that  $k'$  is not a free parameter. It can be fixed by imposing that the definitions of the scaling variables (9) and

(14) coincide at  $\sigma=0$  and  $c=0$ . Thus  $k' = (A-1)/(B-1)$ . The only free parameter for the collapse of the data is  $B$ . Best collapses are shown in Figs. 12 and 13 for  $N_1$  and  $N_2$ , respectively, using the best choice  $B = -0.2$  (thus  $k' = 1$ ).

The continuous lines in both figures correspond to the same lines as in Figs. 10 and 11. We can thus conclude that we have built up two good approximations [given by Eqs. (9) and (14)] to the unique scaling variable in regions I and II which will display a more complex behavior in the intermediate region where the critical line bends, probably with higher order terms.

## VI. DISCUSSION

In this section we will try to explain why the critical line exhibits such a curvature. There must be a physical reason that goes beyond the mere effect of the dilution of the system and destabilizes the phase even more with the ferromagnetic-like discontinuity. We propose that the effect is related to the percolation of vacancies above  $c_p = 0.3116$ , a value which is, indeed, very close to the limit where the critical line loses its linearity. To justify this hypothesis numerically, we have studied the distribution of the clusters of vacancies and the position of the avalanches for each particular realization of disorder. In particular, we have determined the spatial position of the largest vacancy cluster (which, above  $c_p$ , will correspond to the percolating cluster in the thermodynamic limit). It is clear that the neighboring sites of this percolating cluster of vacancies are an easy path for the propagation of an avalanche, since these sites have a smaller number of neighbors. To distinguish such sites we have defined a local flag that takes values  $b_i = 1$  when a site belongs to the border of the largest cluster of vacancies or  $b_i = 0$  otherwise. We have also recorded the largest avalanche during the  $H$  scan (which will correspond to the spanning avalanche below the critical line in the thermodynamic limit) and we have marked its position with a flag  $\epsilon_i = 1$ . With these two variables we have defined the correlation between the border of the largest cluster of vacancies and the largest avalanche as

$$\rho_{\epsilon, b} = \frac{\left\langle \frac{1}{N} \sum \epsilon_i b_i \right\rangle - \left\langle \frac{1}{N} \sum \epsilon_i \right\rangle \left\langle \frac{1}{N} \sum b_i \right\rangle}{\sqrt{\left\langle \frac{1}{N} \sum \epsilon_i^2 \right\rangle - \left\langle \frac{1}{N} \sum \epsilon_i \right\rangle^2} \sqrt{\left\langle \frac{1}{N} \sum b_i^2 \right\rangle - \left\langle \frac{1}{N} \sum b_i \right\rangle^2}}. \quad (15)$$

Note that since  $\epsilon_i$  and  $b_i$  only take values of 1 and 0, the power 2 in the first bracket inside the square roots can be suppressed. This correlation is equal to 1 when the spanning avalanche sits exactly on the border of the spanning cluster of vacancies. The behavior of  $\rho_{\epsilon, b}$  as a function of  $c$  is shown in Fig. 14 for three different values of  $\sigma$  that correspond to the dashed lines indicated in Fig. 9, and for increasing sys-

tem sizes as indicated by the legend. The important observation is that the curves for  $\sigma=0.5$  and  $\sigma=0.1$  exhibit two crossing points. One is located at  $c_p$  and the other on the critical line (it thus shifts with  $\sigma$ ). For a concentration of vacancies below  $c_p$  or above the critical line, the behavior of the curves with increasing  $L$  indicates that the correlation vanishes in the thermodynamic limit, whereas in the region

between the two crossing points the correlation increases with increasing system size. A value  $\rho=1$  is probably not reached, since the spanning avalanche is larger than the border of the percolating cluster of vacancies. Using this analysis, we have thus identified the origin of the curvature of the critical line; when vacancies percolate, the spanning avalanche propagates along the border of the percolating cluster of vacancies. The propagation in such a constrained environment decreases the amount of disorder needed to break the infinite macroscopic avalanche into small microscopic jumps. However, as shown in Sec. V, this mechanism does not change the values of the critical exponents.

## VII. SUMMARY AND CONCLUSIONS

We have analyzed the influence of dilution on the critical properties of the 3D-RFIM at  $T=0$  with metastable dynamics. We have shown that the critical point, associated with the change in the shape of the hysteresis loop from discontinuous to continuous loops, becomes a critical line which we have located on the  $\sigma$ - $c$  phase diagram. The critical proper-

ties close to this line are characterized by the same critical exponents as in the nondiluted model. This result indicates that it should be possible to find RG arguments, showing that there is a unique fixed point at  $T=0$  in the disorder parameter space that includes, at least, both random fields and dilution.<sup>2</sup> We have computed quadratic approximations to the scaling variable in two different zones of the phase diagram that allow for a bivariate finite-size-scaling collapse on a universal scaling function. Finally, we have proposed an explanation for the curvature observed in the critical line when the concentration of vacancies increases above the percolation limit; the spanning avalanche that is responsible for the discontinuity of the hysteresis loops has a tendency to follow the neighborhood of the percolating cluster of vacancies.

## ACKNOWLEDGMENTS

We acknowledge fruitful discussions with M. L. Rosinberg, F. J. Pérez-Reche, and A. Planes. This work has received financial support from projects MAT2004-01291 (CICYT, Spain) and SGR-2001-00066 (Generalitat de Catalunya). X.I. acknowledges a grant from DGI-MEC (Spain).

\*Electronic address: xit@ecm.ub.es

†Electronic address: eduard@ecm.ub.es

<sup>1</sup>J. P. Sethna, K. Dahmen, S. Kartha, J. A. Krumhansl, B. W. Roberts, and J. D. Shore, Phys. Rev. Lett. **70**, 3347 (1993).

<sup>2</sup>J. P. Sethna, K. Dahmen, and O. Perković, *The Science of Hysteresis* (Elsevier Inc., New York, 2005), Vol. 2, Chap. 2, pp. 107–179.

<sup>3</sup>J. Ortín, A. Planes, and L. Delaey, *The Science of Hysteresis* (Elsevier Inc., New York, 2005), Vol. 3, Chap. 5, pp. 467–541.

<sup>4</sup>F. Detcheverry, E. Kierlik, M. L. Rosinberg, and G. Tarjus, Phys. Rev. E **68**, 061504 (2003).

<sup>5</sup>B. Tadić, Eur. Phys. J. B **28**, 81 (2002).

<sup>6</sup>K. A. Dahmen and J. P. Sethna, Phys. Rev. Lett. **71**, 3222 (1993).

<sup>7</sup>K. A. Dahmen and J. P. Sethna, Phys. Rev. B **53**, 14872 (1996).

<sup>8</sup>D. Dhar, P. Shukla, and J. Sethna, J. Phys. A **30**, 5259 (1997).

<sup>9</sup>X. Illa, J. Ortín, and E. Vives, Phys. Rev. B **71**, 184435 (2005).

<sup>10</sup>X. Illa, P. Shukla, and E. Vives, Phys. Rev. B **73**, 092414 (2006).

<sup>11</sup>P. S. S. Sabhapandit and D. Dhar, J. Stat. Phys. **98**, 103 (2000).

<sup>12</sup>P. Shukla, Phys. Rev. E **63**, 027102 (2001).

<sup>13</sup>A. Berger, A. Inomata, J. S. Jiang, J. E. Pearson, and S. D. Bader, Phys. Rev. Lett. **85**, 4176 (2000).

<sup>14</sup>J. Marcos, E. Vives, L. Mañosa, M. Acet, E. Duman, M. Morin,

V. Novák, and A. Planes, Phys. Rev. B **67**, 224406 (2003).

<sup>15</sup>K. L. Babcock and R. M. Westervelt, Phys. Rev. Lett. **64**, 2168 (1990).

<sup>16</sup>P. J. Cote and L. V. Meisel, Phys. Rev. Lett. **67**, 1334 (1991).

<sup>17</sup>E. Vives and A. Planes, Phys. Rev. B **50**, 3839 (1994).

<sup>18</sup>W. Wu and P. W. Adams, Phys. Rev. Lett. **74**, 610 (1995).

<sup>19</sup>Ll. Carrillo, Ll. Mañosa, J. Ortín, A. Planes, and E. Vives, Phys. Rev. Lett. **81**, 1889 (1998).

<sup>20</sup>E. Puppin, Phys. Rev. Lett. **84**, 5415 (2000).

<sup>21</sup>G. Durin and S. Zapperi, Phys. Rev. Lett. **84**, 4705 (2000).

<sup>22</sup>M. P. Lilly, P. T. Finley, and R. B. Hallock, Phys. Rev. Lett. **71**, 4186 (1993).

<sup>23</sup>B. Tadić, Phys. Rev. Lett. **77**, 3843 (1996).

<sup>24</sup>M. C. Kuntz, O. Perković, K. A. Dahmen, B. Roberts, and J. P. Sethna, Comput. Sci. Eng. **1**, 73 (1999).

<sup>25</sup>F. J. Pérez-Reche and E. Vives, Phys. Rev. B **67**, 134421 (2003).

<sup>26</sup>F. J. Pérez-Reche and E. Vives, Phys. Rev. B **70**, 214422 (2004).

<sup>27</sup>O. Perković, K. A. Dahmen, and J. P. Sethna, cond-mat/9609072 (unpublished).

<sup>28</sup>For a discussion of the problems in the nondiluted 2D RFIM, see Ref. 27.